# Rain-wind induced vibrations of cables in laminar and turbulent flow

U. Peil[†] and O. Dreyer[‡]

*Institute for Steel Structures, Technical University, Braunschweig, Germany*

**Abstract.** In the last decades there have been frequent reports of oscillations of slender tension members under simultaneous action of rain and wind - characterized by large amplitudes and low frequencies. The members, e.g. cables of cable-stayed bridges, slightly inclined hangers of arch bridges or cables of guyed-masts, show a circular cross section and low damping. These rain-wind induced vibrations negatively affect the serviceability and the lifespan of the structures. The present article gives a short literature review, describes a mathematical approach for the simulation of rain-wind induced vibrations, sums up some examples to verify the calculated results and discusses measures to suppress the vibrations.

**Keywords:** cable vibration; rain; wind; numerical simulation; aeroelastic instability.

## 1. Introduction

Hikami (1986) measured large cable vibrations during the erection phase of the Meikonishi Bridge near Nagoya in Japan. He was the first person to have noticed and reported on a relationship between cable oscillations, wind and water rivulets on polyethylene-coated cables. On the basis of observations, he assumed the excitation mechanism to be comparable to the aeroelastic galloping instability. He examined the main parameters and properties of rain-wind induced vibrations, like wind speed, wind direction, rain intensity, vibration amplitudes and vibration frequencies, by means of additional wind tunnel tests. With the same method, Matsumoto (Matsumoto, *et al.* 1990, Matsumoto, *et al.* 1995, Matsumoto, *et al.* 1999) confirmed that the upper rivulet on the cross section is the main cause for vibrations with large amplitudes. Saito, *et al.* (1994) described the reduced likelihood of rain-wind induced cable vibrations in turbulent wind flow.

The Erasmus Bridge in Rotterdam (Geurts and van Staalduinen 1999) and the Fred Hartman Bridge in Houston, Texas (Main and Jones 1999) have been affected by rain-wind induced vibrations as well. One year after the opening of the Elbe Bridge near Doemitz (Fig. 1a) fatigue cracks appeared at some hanger nodes (Fig. 1b). These were caused by strong vibrations of the damaged hangers during moderately rainy and windy conditions (Luesse, *et al.* 1996).

The main aspects of rain-wind induced vibrations described in the fore-mentioned publications can be summarized as follows:

† Professor, Corresponding Author, E-mail: u.peil@arcor.de
‡ Dr.-Ing., E-mail: oliver.dreyer@mt-aerospace.de

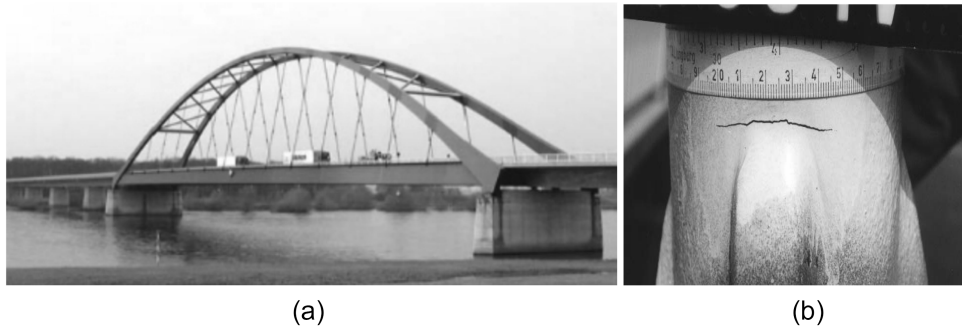(a)                                                                      (b)

Fig. 1 (a) Elbe Bridge near Doemitz, (b) Fatigue crack at hanger node

The oscillations mainly occur in moderately rainy weather, in a limited range of wind angle of attack, in a limited range of wind speed, and they only affect cables with low structural damping. The affected cables vibrate in one or several of the lower modes with low amplitudes in the wind direction, and values several times the cable diameter perpendicular to that direction

Rain-wind induced vibrations can occur when rain drops form axial water rivulets on the round surface of cables or hangers. The rivulets represent separation points for the surrounding wind flow. Thus the fluid pressure distribution is modified, compared with the pressure around a normal circular cross section. The resulting forces cause severe vibrations of the structures. Due to these oscillations and the wind forces, the rivulets move circumferentially on the surface of the structures, and the fluid pressure distribution around the cross section changes. The forces on the structure change and the excitation continues.

The existing simulation approaches of Peil and Nahrath (2003) and Yamaguchi (1990) are based on this excitation mechanism for rain-wind induced vibration. Like other authors, they use a two-dimensional two(three)-mass-oscillator with two(four) degrees of freedom (Fig. 2). The cable can move translationally in (horizontal and) vertical direction. The cable mass is viscously damped and supported by springs. The (two) rivulet(s) move(s) circumferentially on the cable surface. The masses of the rivulets are coupled with the cable mass. Like a driven pendulum, they swing around the moving centre of the cable's cross-section. Damper elements simulate the frictional resistance between the rivulets and the cable's surface. The wind forces and moments act in the direction of the degrees of freedom.
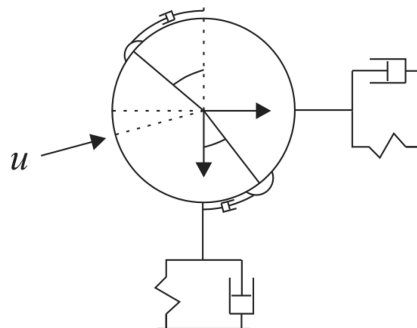


Fig. 2 Two-dimensional three-mass-oscillator with four degrees of freedom (Nahrath 2003)

In this paper, Nahrath's model is enhanced by investigations on a cable in 3D space. In addition, the behaviour of the rivulets is examined in more detail by numerical simulations using simplified Navier-Stokes equations, and the turbulent wind flow is considered. The approach is able to simulate the oscillation amplitudes, frequencies and other main properties (Peil and Nahrath 2003b, Dreyer 2005). The calculation in the time domain allows for all nonlinear aspects. The model consists of three components: the equations of dynamic motion of a sagged cable, the equations of motion of the rivulets and the computation of the aerodynamic forces in laminar and turbulent flow, depending on the rivulet positions on the cable surface. The calculated results are verified on the basis of test data. Possible measures to suppress rain-wind induced vibrations are discussed.

Apart from the above-mentioned theory, which represents a self-induced excitation mechanism, other authors present different explanations and mathematical models for rain-wind induced vibrations. Van der Burgh and Abramian (2002) analyse a two-dimensional oscillator with a coupled rivulet mass that changes harmonically in the course of vibration. Geurts and van Staalduinen (1999) use an adjusted galloping model to calculate the cable vibrations and the damping measures of the Erasmus Bridge in Rotterdam. Seidel and Dinkler (2004) assume that the rivulet movement on the cable surface causes a change between the sub-critical and the super-critical separation of the wind flow around the circular cable section. This theory can explain the cable vibration in the direction of the wind flow, but seems to be unsuitable for lateral vibrations. An empirical approach to calculating lateral cable vibrations induced by rain and wind is presented by Schwarzkopf and Sedlacek (2005). Their model uses aerodynamic coefficients determined in wind tunnel tests in order to calibrate a so-called critical velocity at which the measured cable vibrations are reproduced. This model seems to be valid only within the scope of the investigated parameter range. The critical velocity is not identical with the onset wind speed of rain-wind induced vibrations. It can deviate from the real wind speed by a factor of three or more. Thus the critical wind speed cannot be used for the determination of fatigue assessment.

## 2. Equations of motion for the cable

Horizontal and inclined cables sag due to their dead weight. The excited structure oscillates around the static position that can be approximately described by a quadratic parabola in case of a taut cable.

In order to derive the equations of motion for the sagged cable in 3D space (Fig. 3a), the equilibrium conditions of the external and internal forces acting on an element of the oscillating cable (Fig. 3b) are formulated (Eq. 1: direction 1). They include the inertia forces, the external forces and the cable forces (Lazarides 1985).

$$\left( S_d + \frac{\partial S_d}{\partial s_d} ds_d \right) \cos\left( \alpha_1 + \frac{\partial \alpha_1}{\partial s_d} ds_d \right) - S_d \cos \alpha_1 + f_{d1} ds_d - \mu_d ds_d g \sin\delta = 0 \tag{1}$$

With the terms

$$\cos\left( \alpha_1 + \frac{\partial \alpha_1}{\partial s_d} ds_d \right) = \cos \alpha_1 \cos\frac{\partial \alpha_1}{\partial s_d} ds_d - \sin \alpha_1 \sin\frac{\partial \alpha_1}{\partial s_d} ds_d$$

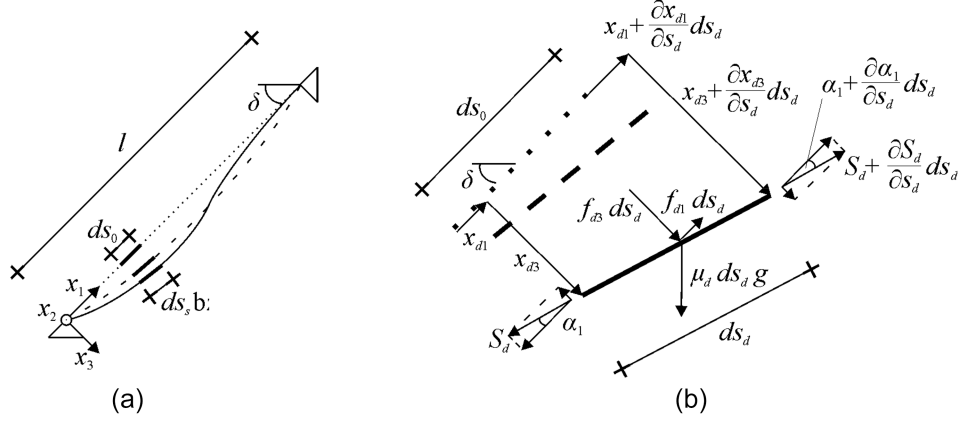$$= \cos \alpha_1 - \sin \alpha_1 \frac{\partial \alpha_1}{\partial s_d} ds_d \tag{2}$$

Fig. 3 (a) Sagged cable in 3D space, (b) Cable element

$$\mu_0 ds_0 = \mu_d ds_d \Rightarrow \mu_d = \mu_0 \frac{ds_0}{ds_d} \tag{3}$$

$$\varepsilon_d = \frac{S_d}{EA} \Rightarrow ds_d = (1 + \varepsilon_d) ds_0 \tag{4}$$

$$S_d = S_s + S \tag{5}$$

$$\varepsilon = \frac{S}{EA} \Rightarrow ds_d = (1 + \varepsilon) ds_s = \left(1 + \frac{S}{EA}\right) ds_s \tag{6}$$

$$q_{s1} = -\mu_s g \sin \delta \tag{7}$$

$$-\mu_d g \sin \delta = -\mu_s g \sin \delta \frac{ds_s}{ds_d} = q_{s1} \frac{ds_s}{ds_d} \quad \text{and} \tag{8}$$

$$q_1 - \mu_d \frac{\partial^2 x_{d1}}{\partial t^2} = f_{d1} \tag{9}$$

and some simplification steps, the calculation produces the equations of motion for $i = 1$ and the remaining directions (Eq. 10).

$$\frac{\partial}{\partial s_0}\left(\frac{S_d}{1 + \varepsilon_d}\frac{\partial x_{di}}{\partial s_0}\right) + \frac{1 + \varepsilon_d}{1 + \frac{S}{EA}} q_{si} + (1 + \varepsilon_d) q_i - \mu_0 \frac{\partial^2 x_{di}}{\partial t^2} = 0 \qquad i = 1, 2, 3 \tag{10}$$

where $\mu$−cable mass per unit length; $S$−cable tension; $EA$−axial stiffness of the cable cross section; $\varepsilon$−strain; $g$−gravity; $\delta$−cable inclination; $f$, $q$−external static and dynamic loads; $t$−time; $s$−curvilinear coordinate along the cable; $x_i$−displacement of the cable and $i$−directions. While the indices stand for the initial (0), static (s) and dynamic (d) state of the oscillating cable, the

difference of the variables in the static and dynamic state is denoted by letters without index. The wind forces $q_i$ on the cable in direction $i$ are calculated with the help of the components $\bar{q}_D$ and $\bar{q}_L$ (Eq. 20).

In order to determine the four unknown variables $x_i$ and $S$ in every step of the time domain analysis, the equation of continuity (Eq. 11) is added to the set of equations.

$$\sqrt{\sum_i \left(\frac{\partial x_{d,i}}{\partial s_0}\right)^2} - (1 + \varepsilon_d) = 0 \tag{11}$$

## 3. Equation of motion for the rivulets

The water rivulets have an important influence on the excitation of rain-wind induced vibrations. Due to the complex interaction between air and water on the solid surface most authors use a swinging pendulum that is coupled with the cable as an approximation (e.g. Nahrath 2003 and Yamaguchi 1990).

In this paper, the rivulet flow is described with simplified two-dimensional equations of fluid motion in the circumferential direction of the cable section.

The flow of a fluid can be simulated with the Navier-Stokes equations and the corresponding equation of continuity. With the assumption that the height of the rivulet is small compared with its lateral extent (Fig. 4: $h \ll 2a$), the velocity parallel to the solid surface is clearly bigger than the component in the perpendicular direction. Neglect of the small terms in the Navier-Stokes equations and the associated equation of continuity can simplify the equations considerably (Eq. 12), (Hocking 1980).

$$\frac{\partial p}{\partial \bar{z}} = \rho_w(-g \cdot \cos\beta + f_{\bar{z}} + b_{\bar{z}})$$

$$\frac{\partial p}{\partial \bar{y}} = \mu\frac{\partial^2 \bar{v}}{\partial \bar{z}^2} + \rho_w(g \cdot \sin\beta + f_{\bar{y}} + b_{\bar{y}})$$

$$\frac{\partial \bar{v}}{\partial \bar{y}} + \frac{\partial \bar{w}}{\partial \bar{z}} = 0 \tag{12}$$

where $p$ – pressure; $\rho_w$ – density of the fluid; $\mu$ – viscosity; $f_i$ and $b_i$ – external forces and accelerations of the cable; $\bar{y}$, $\bar{z}$, $\bar{v}$, $\bar{w}$ – displacements and velocities (Fig. 4); $g$ – gravity; $\beta$ – inclination of the tangent plane to the cable surface and $f_i$, $b_i$ – external forces and cable accelerations. The wind forces on the rivulet are calculated by $f_i = \bar{q}_{M,i}/r$ (Eq. 20); $r$ = cable radius), the acceleration terms are taken
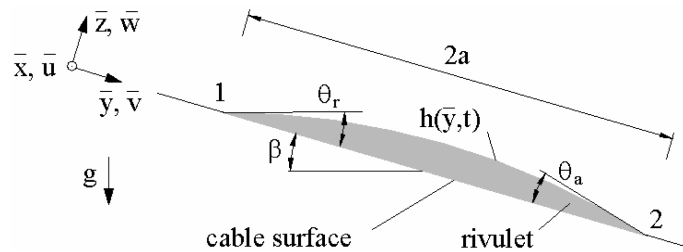


Fig. 4 Rivulet on an inclined surface

from Eq. (10) ($b_i = \partial^2 x_{di}/\partial t^2$), while the adhesion is considered with the help of the slip coefficient $\lambda$ (Eq. 13). The boundary conditions on the cable and the rivulet surface are

$$\bar{z} = 0: \quad \bar{w} = 0$$

$$\bar{v} = \lambda \frac{\partial \bar{v}}{\partial \bar{z}} \tag{13}$$

$$\bar{z} = h(\bar{y}, t): \quad \frac{\partial \bar{v}}{\partial \bar{z}} = 0$$

$$\frac{\partial h}{\partial t} + \bar{v}\frac{\partial h}{\partial \bar{y}} = \bar{w}$$

$$p + \sigma\frac{\partial^2 h}{\partial \bar{y}^2} = const. \tag{14}$$

where $h$ − rivulet height; $t$ − time; $\lambda$ − slip coefficient; $\sigma$ − surface tension (Fig. 4). The tangential stress vanishes at the interface between rivulet and the surrounding air (Eq. 8). In addition, the normal stress must be continuous across $\bar{y} = h$. Due to the surface tension at the contact line between gas, liquid and solid (Fig. 4: points 1 and 2), a static contact angle $\theta_0$ can be observed. If the interface moves, the contact angle $\theta_2$ at the advancing edge grows, while the angle $\theta_1$ at the retreating edge becomes smaller. This fact is formulated as follows:

$$\text{boundary 1: } \left(\frac{\partial h}{\partial \bar{y}}\right)_1 = \begin{cases} \theta_1, \text{ if } \bar{v}_1 > 0 \\ \theta_2, \text{ if } \bar{v}_1 < 0 \end{cases} \qquad \text{boundary 2: } -\left(\frac{\partial h}{\partial \bar{y}}\right)_2 = \begin{cases} \theta_2, \text{ if } \bar{v}_2 > 0 \\ \theta_1, \text{ if } \bar{v}_2 < 0 \end{cases}$$

$$\theta_1 < \left(\frac{\partial h}{\partial \bar{y}}\right)_1 < \theta_2, \text{ if } \bar{v}_1 = 0 \qquad \theta_1 < -\left(\frac{\partial h}{\partial \bar{y}}\right)_2 < \theta_2, \text{ if } \bar{v}_2 = 0 \tag{15}$$

With the given boundary conditions, the calculation of the pressure and velocity components results in the equation of motion (Eq. 16) for the rivulet on the cable surface (e.g. Dreyer 2005, and Hocking 1980).

$$\frac{\partial h}{\partial t} + \frac{\sigma}{3\mu}\frac{\partial}{\partial \bar{y}}\left[h^2(h + 3\lambda)\left(\frac{\partial}{\partial \bar{y}}\left(\frac{\partial^2 h}{\partial \bar{y}^2} + \frac{\rho_w(f_{\bar{z}} + b_{\bar{z}} - g\cos\beta)}{\sigma}h\right) + \frac{\rho_w(f_{\bar{y}} + b_{\bar{y}} + g\sin\beta)}{\sigma}\right)\right] = 0 \tag{16}$$

The no-slip condition on the cable surface is replaced by the Maxwell slip condition (Hocking 1980). The slip coefficient $\lambda$ depends on the material of the cable and its surface conditions (roughness). To determine the slip coefficient, experiments have been carried out. A rotating cylinder is sprinkled by water, the rivulet at the bottom is shifted by the rotation, the displacement of the water rivulet is measured (Fig. 5). Main parameters are the cylinder inclination, the cylinder diameter, the cylinder surface condition, the amount of water and the rotational velocity.

Fig. 6(a) shows some resulting rivulet displacements depending on the cylinder's rotational velocity and angle of inclination $\delta$. The diameter of the polyethylene tube was 100 mm and the water rate was $q_r = 1{,}0$ mm per minute.

In order to determine the slip coefficient, the following procedure was used: The calculation on the tangential plane starts with a conversion of the angular velocity to the dimension (m/s). With an estimated

Fig. 5 (a) Rotating cylinder, (b) Displaced rivulet on the cylinder bottom
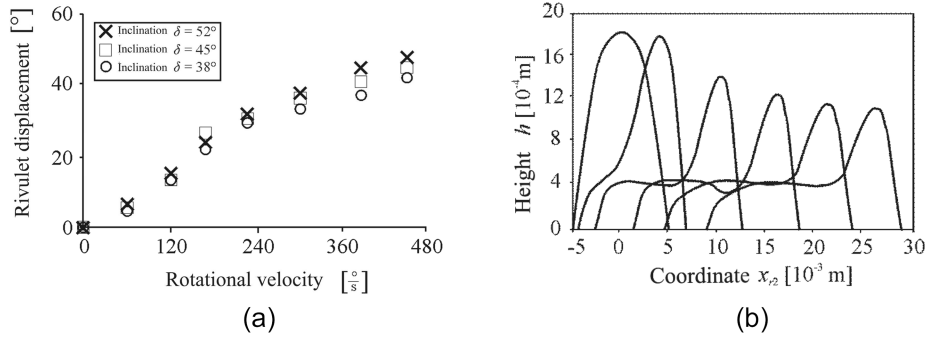


Fig. 6 (a) Test results, (b) Rivulet shape and position

value for $\lambda$, the solution of the equation of motion results in a rivulet velocity for every test. This procedure is repeated until a defined maximum offset between measured and calculated values is reached.

A sample calculation with the parameters $\rho_w = 1{,}000$ kg/m$^3$, $\mu = 1.8 \cdot 10^{-5}$ Ns/m$^2$, $\sigma = 0.073$ N/m, $\lambda = 1.7 \cdot 10^{-6}$ m, $2a = 0.01$ m, $\theta_0 = 0.1$, $\theta_1 = 0.09$ and $\theta_2 = 0.12$ illustrates the changing rivulet shapes and positions with time as described in the given rivulet equation. A quadratic parabola is assumed to be the initial shape of the rivulet (Fig. 6b).

## 4. Aerodynamic forces

It is assumed that the rain-wind induced forces are self-induced and-in the relevant wind velocity range-independent of the Reynolds-Number. The quasi-steady strip assumption (Nahrath 2003 and Yamaguchi 1990) is used.

The three-dimensional orientation of the cable results in an angle $\beta$ and an effective wind velocity $u_{rel}$ ($\approx u$, see Fig. 7), which depend on the yaw angle $\psi$ and the cable inclination $\delta$.

$$\beta = \arctan\left(\frac{(u_0 \sin\psi)\sin\delta}{-u_0 \cos\psi}\right) = \arctan(-\tan\psi\,\sin\delta) \qquad (17)$$

$$u = u_0 \sqrt{\cos^2\psi + \sin^2\psi\,\sin^2\delta} \qquad (18)$$

$$\alpha_I = -\vartheta_1 + \arctan\left(\cfrac{\cfrac{x_3}{\partial t} + \cfrac{r}{d}\cfrac{\partial \vartheta_1}{\partial t}\sin\vartheta_1}{u - \cfrac{x_2}{\partial t} + \cfrac{r}{d}\cfrac{\partial \vartheta_1}{\partial t}\cos\vartheta_1}\right)$$

$$\cong -\vartheta_1 + \frac{1}{u}\frac{\partial x_3}{\partial t} + \frac{1}{2u}\frac{\partial \vartheta_1}{\partial t}\sin\vartheta_1$$

$$\alpha_{II} \cong +\vartheta_2 - \frac{1}{u}\frac{\partial x_3}{\partial t} + \frac{1}{2u}\frac{\partial \vartheta_2}{\partial t}\sin\vartheta_2 \tag{19}$$

The wind forces plotted in Figs. 7 and 8 are the product of the pressure and the aerodynamic coefficients $C$, where $q$−aerodynamic forces and moments; $\rho_l$−density of air; $d$−cable diameter and $\alpha$−angle of attack (Eq. 19, 20). The aerodynamic coefficients depend on the cable movements $x_i$, the position $\vartheta$ and velocity of the rivulets and on the angle $\beta$ as shown in Fig. 7.

$$\bar{q}_D = \frac{1}{2}\rho_l d u_{rel}^2 C_D(\alpha_I,\ \alpha_{II})$$

$$\bar{q}_L = \frac{1}{2}\rho_l d u_{rel}^2 C_L(\alpha_I,\ \alpha_{II})$$

$$\bar{q}_{M1} = \frac{1}{2}\rho_l d^2 u_{rel}^2 C_{M1}(\alpha_I,\ \alpha_{II})$$

$$\bar{q}_{M2} = \frac{1}{2}\rho_l d^2 u_{rel}^2 C_{M2}(\alpha_I,\ \alpha_{II}) \tag{20}$$
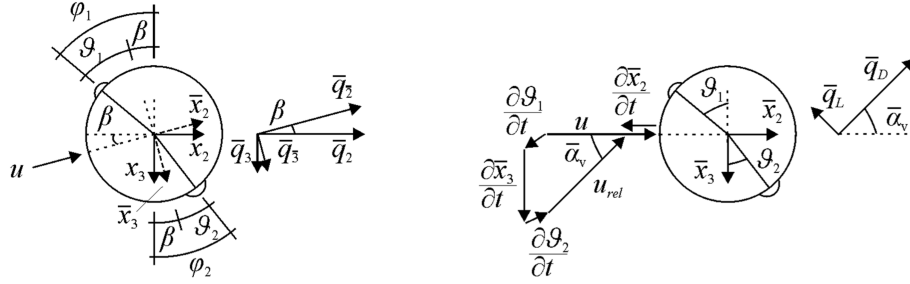

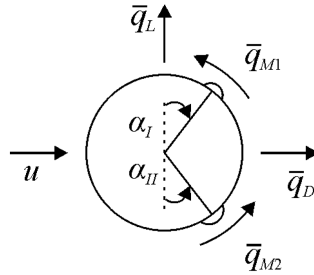
Fig. 7 Wind forces acting on cable section



Fig. 8 Angles of attack

Fig. 7 and Eqs. (17) to (20) are valid in laminar wind flow (i.e. constant wind velocity) only. In turbulent conditions, correlated fluctuating components in all directions (Eq. 21) are added to the mean wind velocity profile that is a function of the height above ground (Davenport 1961). The lengthy description of the generation of these values is given by Wang (1994) based on the work of Shinozuka (1971).

$$u_{01}(t) = \bar{u}_{01} + u'_{01}(t)$$
$$u_{02}(t) = u'_{02}(t)$$
$$u_{03}(t) = u'_{03}(t) \tag{21}$$

For evaluation of the aerodynamic coefficients ($C_D$, $C_L$, $C_M$), wind tunnel tests have been carried out with a full-scale model. The quasi-steady wind forces were measured on a 1 m cylinder with a diameter of 10 cm. Axial strips were attached to a cylinder in order to simulate the rivulets. The strips had circular arched cross sections with a height of 3 mm and a width of 10 mm. Cylinders with one (upper) and two rivulets were tested at a wind velocity of $u = 10$ m/s. The Reynolds-Number $Re = 70000$ is sub-critical for an undisturbed circular section. It shows only a slight interdependence of wind velocity and aerodynamic coefficients. Apart from the afore-mentioned conditions concerning the dimensions and the Reynolds-Number, the tests in turbulent flow require a certain scale between the dimensions of the turbulent gust balls and the diameter of the cylinder. This scale could not be simulated in the wind tunnel, because the axial strips representing the rivulets would have been too small.

Fig. 9 shows, for instance, the influence of the angle of attack on the lift coefficient at different turbulence intensities. The higher the turbulence intensity, the lower the peaks in the turbulent coefficient curves in comparison with laminar conditions.
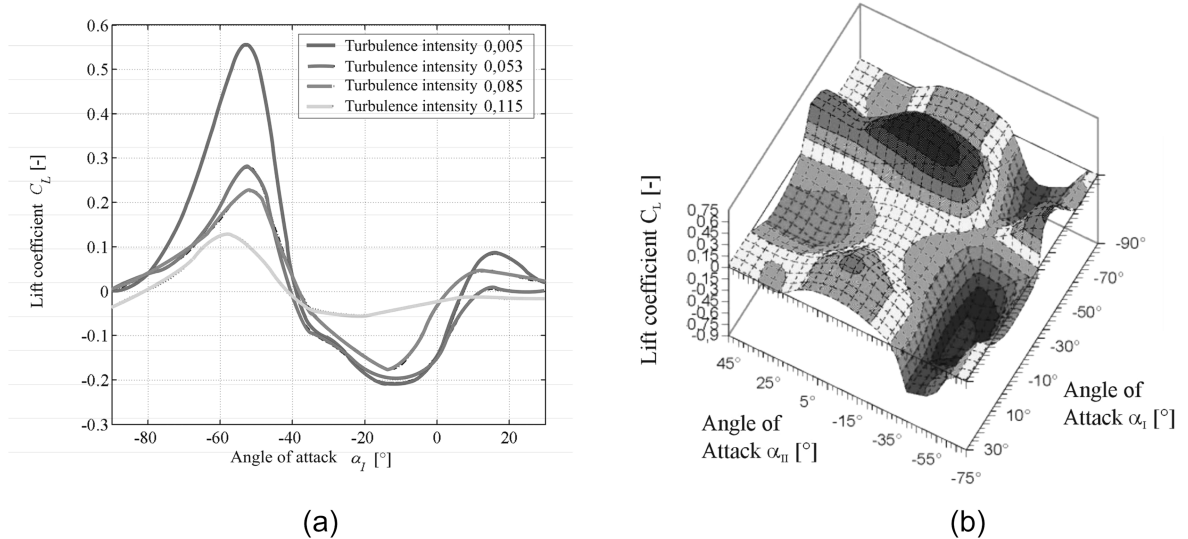


(a)                                                    (b)

Fig. 9 (a) Aerodynamic lift coefficient, 1 rivulet, various turbulence intensities, (b) Aerodynamic lift coefficient, 2 rivulets ($\alpha_I$ – upper rivulet, $\alpha_{II}$ – lower rivulet), laminar

## 5. Excitation mechanism and some results

### 5.1. Complete procedure

In order to simulate the described excitation mechanism, the components explained in Sections 2 to 4 are joined to form a complete model. The analysis of the structure's equations of motion results in displacements, velocities and accelerations of the cable nodes. The latter cause inertia forces that act on the rivulet-in addition to the wind and adhesion forces. Shape, position and velocity of the rivulets are calculated by means of the equation of motion for the rivulets on the cable surface. These positions represent the separation points for the wind flow around the cable section. With this input information, the aerodynamic coefficients and the wind forces for the next time step are determined. Each calculation starts with the calculation of the stationary rivulet positions and a small perturbation in the time domain analysis with the help of the Newmark's procedure. The cables are divided into approx. 10 elements and the rivulet surfaces are divided into approx. 30 segments. Due to the high number of degrees of freedom, the simulation is very time-consuming in comparison to the (Nahrath 2003) model.

This description of the complete procedure clearly shows that the cable motion (Eq. 10) is coupled to the rivulet motion (Eq. 16). Moreover, the aerodynamic coefficients depend on the cable and rivulet motion (Eq. 19, Fig. 7). The relevant terms are explained in Sections 2 to 4.

### 5.2. Excitation mechanism and unstable velocity range

An example of measured vibrations of the Fred Hartman Bridge is used for the calculation (Zuo and Jones 2003, Main and Jones 1999), with the parameters $d=0.19$ m, $\mu=95$ kg/m (mass per length), $\delta=28,5^\circ$, $l=172$ m (cable length), $S_s=5100$ kN, $\xi=0,0015$ (damping coefficient) and $f_1=0.625$ Hz (eigenfrequency) for the cable, as well as $\rho_w=1000$ kg/m$^3$ (density), $\sigma=0.0735$ N/m, $\lambda=1.7*10^6$ m, $\mu=1.0*10^6$ m$^2$/s and $a_0=0.006$ m for the rivulets. The wind speed is $u=11.5$ m/s = const. from direction $\psi=30^\circ$. The calculated time histories of the maximum cable deformation (at $0.5*l$) in directions 2 and 3 are shown in Figs. 10(c) and 10(a), while the time history of the upper rivulet's angle of attack is plotted in Fig. 10(b). Initially, the amplitude steadily increases and the rivulet starts oscillating around its stationary position at the same frequency. After approximately 400 s, an equilibrium state with steady amplitudes is reached. It is important to note that the equilibrium state is reached when the upper angle of attack reaches about $-55^\circ$. The aerodynamic lift coefficients show large gradients in the angle range of about $\alpha_l=-45^\circ$ and changing signs of the gradients at $\alpha_l=-55^\circ$ (Fig. 9). When having in mind the den Hartog-criterion (1952) for the proneness of cross sections to galloping excitation, this effect is understandable.

The alteration of the aerodynamic forces and of the cable deformation shows the same frequency. The product of force and velocity is positive most of the time. Due to that the work per period, i.e., the integral of work over the time, is always positive and thus the vibration amplitudes grow.

One of the main characteristics of rain-wind induced vibrations is the limited unstable wind velocity range (see Fig. 10e). When a critical minimum wind velocity has been exceeded, the amplitudes quickly grow. After reaching their maxima, the amplitudes decrease. They stop when a critical maximum wind velocity has been reached. Fig. 10(e) shows that for a wind speed $u=8.8$ m/s, the amplitude in direction 3 $x_{d3}$ is 0.30 m. The other degrees of freedom are calculated, but not
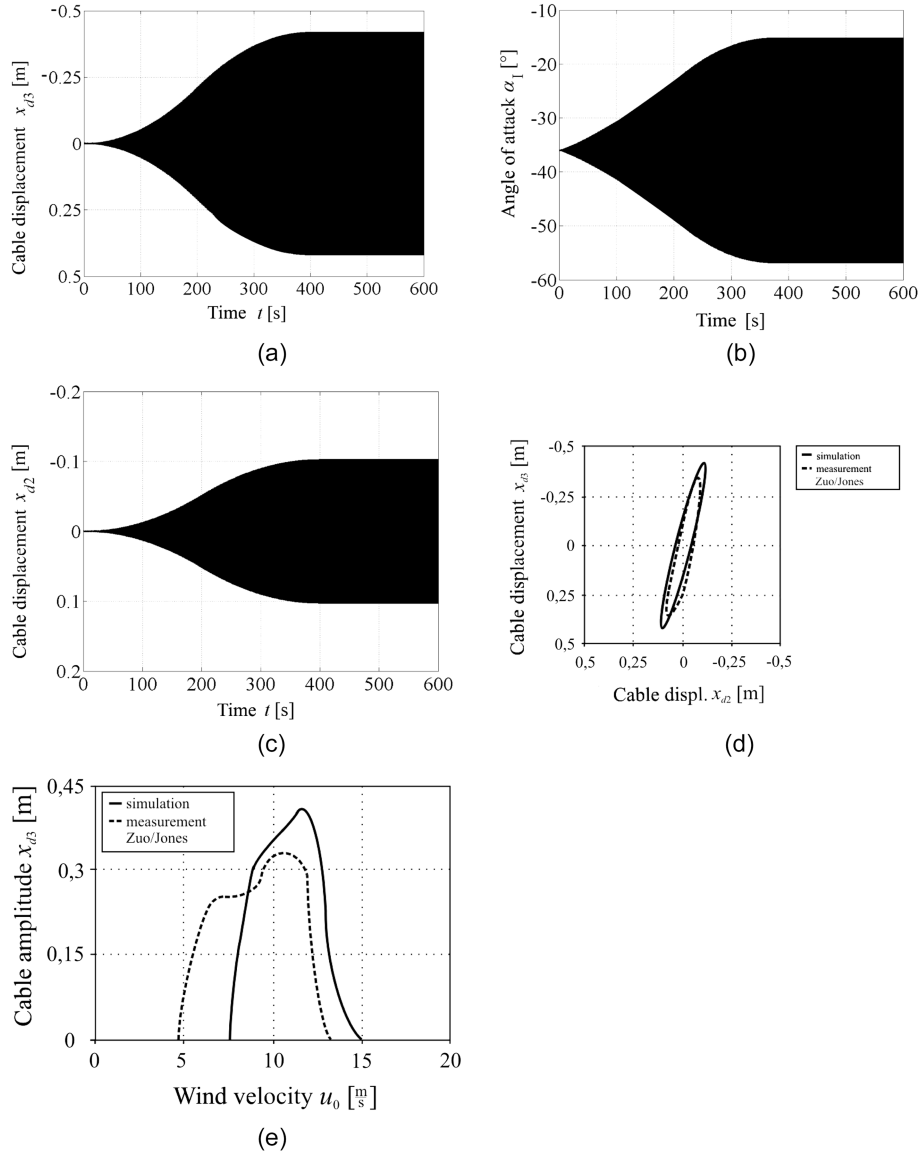
Fig. 10 (a) Time history of cable deformation in direction 3, (b) Time history of the upper angle of attack, (c) Time history of cable deformation in direction 2, (d/e) Comparison: simulation results and observation data Zuo and Jones (2003) and Main and Jones (1999), calculated results given at 0.5*l.

plotted in this paper. If $u = 11.5\,\text{m/s}$, the maximum amplitude $x_{d3} = 0.42\,\text{m}$ is reached. With the changing wind velocity, the initial angle of attack shifts from $\alpha_I = -49°$ to $\alpha_I = -36°$. Thus the change of the angle increases. This affects the cable deformations and the rivulet amplitudes, which both have bigger values. An equilibrium state with steady amplitudes is reached within a longer period of time. When the angle of attack exceeds its critical maximum value, the damping is positive most of the time and the vibration increase becomes less distinct and finally stops. The wind velocity, which is just high enough to prevent the upper rivulet from moving down the cable section windward,
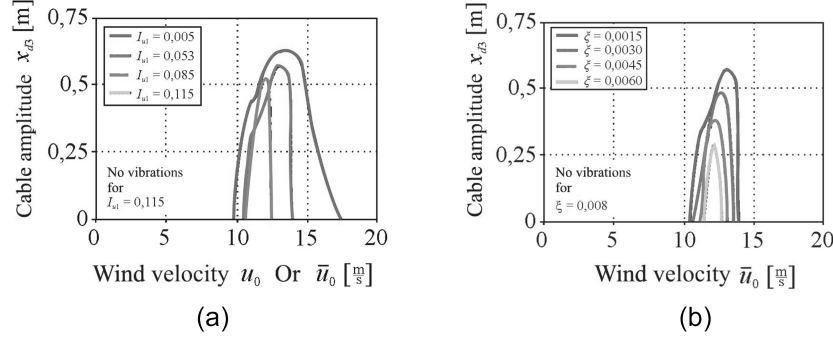
Fig. 11 (a) Unstable wind velocity range for different turbulence intensities, (b) Unstable wind velocity range for different damping coefficients, calculated results given at 0.5*1 and 0.67* 1 .

represents the lower limit of the unstable wind velocity range. In the case of just one lower rivulet (Fig. 12), the cable vibrations are considerably smaller.

The calculated amplitudes and unstable wind velocity range in Figs. 10(d) and 10(e) show a good agreement with observation data published in Zuo and Jones (2003) and Main and Jones (1999). While the observed vibrations occurred in several low cable modes, the presented model only shows cable oscillations in the first mode in laminar wind flow. The given amplitudes refer to the cable sector with maximum displacements.

A second example simulates the rain-wind induced cable vibration observed for the Erasmus Bridge in Rotterdam. The parameters for the cable and the wind are $d=0.21$ m, $\mu=60$ kg/m, $\delta=30°$, $l=250$ m, $\xi=0.0015$, $f_1=0.45$ Hz, $u=14.0$ m/s and $\psi=25°$, whereas the parameters for the rivulets remain unchanged.

It is stated in Geurts and van Staalduinen (1999) that the maximum amplitude in direction 3 was about 0.55 m for the second example. Fig. 11(a) shows that the cable deformation and the unstable wind velocity range decrease in case of a growing turbulence intensity. The increasing wind fluctuation disturbs the rivulet movements. Furthermore, the correlation of the aerodynamic forces along the cable axis is reduced. For a turbulence intensity of about $I_{u1}=0.053$, the calculation results show a good agreement with the measurements. Taking diagram 8a into consideration, one could assume that the amplitude reduction would be larger than calculated. But as already mentioned, the actual geometrical proportions could not be modelled in the wind tunnel, which is due to scaling problems. Because of this there are differences between simulation and measurement.

Again the observed vibrations occurred in several low cable modes, while the presented model shows cable oscillations in the first mode in laminar wind flow (at 0.5*l) and in several low modes in turbulent flow (at 0.67*l). The mean wind profile is described by the power law with an exponent $\alpha=0.3$. Again, the given amplitudes refer to the cable sector with maximum displacements.

Nahrath (2003) calculated a value of $x_{d3}=0.30$ m for the cable amplitude in direction 3 with the two-dimensional model shown in Fig. 2, while taking into account a correlation length of only 50% for the aerodynamic forces along the cable axis.

No sag effects of the vibrating cables were detected. The values of the independent parameter $\lambda_s^2$ are low in both examples (cable of Fred-Hartman Bridge: $\lambda_s^2=0.7$; cable of Erasmus Bridge: $\lambda_s^2=3.3$). The parameter $\lambda_s^2=(\mu\ g\ \cos(\delta)\ l/S)^2 l/(S\ L_e/EA)$ was introduced by Irvine (1992) in order to characterize the behaviour of cables, where $L_e=l\ (1+1/8\ (\mu\ g\ \cos(\delta)\ l/S)^2)$.
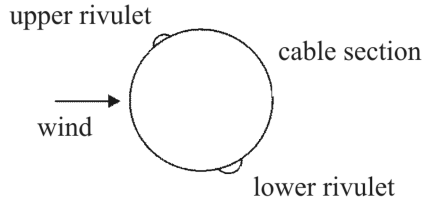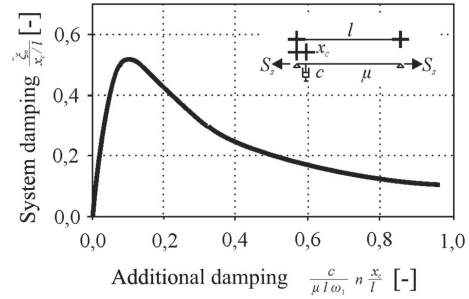
Fig. 12 Rivulets on cable section



Fig. 13 System damping and additional damper constant (Pacheco, *et al.* 1993)

### 5.3. Damping measures

The example of the Erasmus Bridge in Rotterdam can, in addition, be used to examine the effect of cable damping on rain-wind induced vibrations. The cable amplitudes in direction 3 are plotted in Fig. 11(b) for $I_{u1} = 0.053$ and different damping ratios. As a result of increasing damping, the maximum cable amplitudes and the unstable wind velocity ranges become smaller. In order to suppress the rain-wind induced vibrations at the Erasmus Bridge completely, additional dampers with damping constants $c = 2*25$ kNs/m have been installed (Geurts and van Staalduinen 1999). Fig. 12 (Pacheco, *et al.* 1993) allows an overall system damping value of a cable with a given discrete damper to be determined on the basis of a free vibration analysis. When using this diagram and the distance $x_c = 4.2$ m from the support, the sum of structural and discrete damping ratio results in $\xi_{ges} = 0.0015 + 0.4*(4.2/250) = 0.0082$. Corresponding with the observations *in situ* (Geurts and van Staalduinen 1999), the simulation proves that vibrations are prevented, if the damping ratio exceeds 0.008 (Fig. 11b).

## 6. Summary

The present paper describes an approach that allows rain-wind induced cable vibrations to be calculated. It is shown how the interaction between the wind flow, the movements of the cable and the rainwater rivulets lead to self-induced vibration. The calculated results show a good agreement compared with in-situ observation data given in various publications and the simplified two-dimensional model by Nahrath (2003).

Due to the fact that the ratio of the integral length scale of the turbulent eddies of the grid-generated turbulence and the diameter of the cylinder, could not be simulated in the wind tunnel, investigations are continuing to allow for precise consideration of the natural turbulence. Thus, full-scale field tests are being carried out at the moment at the Institute of Steel Structures at the Technical University of Braunschweig. Additional questions requiring clarification relate to the excitation of several cable modes under different conditions, and the assumed independence of the aerodynamic coefficients of the Reynolds number in turbulent flow.

## Acknowledgements

## References

Burgh, A. H. P. V. D. and Abramian, A. K. (2002), "On the modeling of rain-wind induced vibrations of a simple oscillator", *Proceedings of the International Mechanical Engineering Congress & Exposition*, New Orleans, 2002.

Davenport, A. G. (1961), "The application of statistical concepts to the wind loading of structures", *Proceedings*, The Institution of Civil Engineers, London, **19**, 449-472.

den Hartog, J. P. (1952), *Mechanische Schwingungen*, Springer, Berlin Göttingen Heidelberg (in German).

Dreyer, O. (2005), "Regen-Wind induzierte Seilschwingungen in laminarer und turbulenter Strömung", *Dissertation Technische Universität Braunschweig* (in German).

Geurts, C. P. W. and van Staalduinen, P. C. (1999), "Estimation of the effects of rain-wind induced vibration in the design stage of inclined stay cables", *Proceedings of the 10th International Conference on Wind Engineering, Copenhagen*, 885-891.

Geurts, C. P. W., van Staalduinen, P. C., Vrouwenvelder, T. and Reusink, J. (1998), "Numerical modeling of rain-wind induced vibration: Erasmus Bridge, Rotterdam", *Struct. Eng. Int.*, **8**, 129-135.

Hikami, Y. (1986), "Rain vibrations of cables of cable-stayed bridges", *J. Japan Associ. Wind Eng.*, **27**, 17-28.

Hocking, L. M. (1980), "Sliding and spreading of a thin two-dimensional drop", *Quarterly Journal of Mechanics and Applied Mathematics*, **34**, 37-55.

Irvine, M. (1992), "Cable structures", *Proc. Dover Publications*, New York.

Lazaridis, N. (1985), *Zur dynamischen Berechnung abgespannter Maste und Kamine in böigem Wind unter besonderer Berücksichtigung der Seilschwingungen*, Dissertation Universität der Bundeswehr München (in German).

Lüesse, G., Ruscheweyh, H., Verwiebe, C. and Günther, G. H. (1996), "Regen-Wind induzierte Schwingung-serscheinungen an der Elbebrcke Domitz", *Stahlbau*, **65**, 105-114 (in German).

Main, J. A. and Jones, N. P. (1999), "Full-scale measurements of stay cable vibration", *Proceedings of the 10th International Conference on Wind Engineering,* Copenhagen, 963-971.

Matsumoto, M., Saito, T., Masahiko, K., Hiromichi, S. and Nishizaki, T. (1995), "Response characteristics of rain-wind induced vibrations of stay cables of cable-stayed bridges", *J. Wind Eng. Ind. Aerodyn.*, **57**, 323-333.

Matsumoto, M., Shiraishi, N., Kitazawa, M., Knisely, C., Shirato, H., Kim, Y. and Tsujii, M. (1990), "Aerodynamic behaviour of inclined circular cylinders-cable aerodynamics", *J. Wind Eng. Ind. Aerodyn.*, **33**, 63-72.

Matsumoto, M., Yagi, T. and Tsushima, D. (1999), "Vortex induced vibration of inclined cables at high wind velocity", *Proceedings of the 10th International Conference on Wind Engineering*, 979-986.

Nahrath, N. (2003), *Regen-Wind induzierte Schwingungen*, Dissertation Technische Universität Braunschweig (in German).

Pacheco, M. B., Fujino, Y. and Sulekh, A. (1993), "Estimation curve for modal damping in stay cables with viscous damper", *J. Struct. Eng.*, **119**, 1961-1979.

Peil, U. and Nahrath, N. (2003a), "Modelling of rain-wind induced vibrations", *Wind Struct.*, **6**, 41-52.

Peil, U. and Nahrath, N. (2003b), "Modelling of rain-wind induced vibrations", *Proc. 11th Int. Conf. Wind Engineering, Lubbock, Texas* (2003), 389-396.

Saito, T., Matsumoto, M. and Kitazawa, M. (1994), "Rain-wind excitation of cables of cable-stayed Higashi-Kobe Bridge and cable vibration control", *Proceedings of the International Conference of cable-stayed and suspension bridges, Deauville*, 507-514.

Schwarzkopf, D. and Sedlacek, G. (2005), "Regen-wind induzierte Schwingungen [blank] - [blank] Ein Berechnungsmodell auf der Grundlage der neusten Erkenntnisse", *Stahlbau*, **74**, 901-907 (in German).

Seidel, C. and Dinkler, D. (2004), "Phänomenologie und modellierung regen-wind induzierter schwingungen", *Bauingenieur*, **79**, 145-154 (in German).

Shinozuka, M. (1971), "Simulation of multivariate and multidimensional random processes", *J. Acoust. Soc. America.*, **49**, Part 2, 357-367.

Wang, Z.-H. (1994), *Schwingungsverhalten der Abspannseile von Masten unter Berücksichtigung der Böenbelastung*, Dissertation Universität Karlsruhe (in German).

Wang, L. Y. and Xu, Y. L. (2003), "Analytical study of wind-rain induced cable vibration: 2DOF model", *Wind Struct.*, **6**, 291-306.

Yamaguchi, H. (1990), "Analytical study on growth mechanism of rain vibrations", *J. Wind Eng. Ind. Aerodyn.*, **33**, 73-80.

Zuo, D. and Jones, N. P. (2003), "Interpretation of observed damper performance in mitigating wind and rain-wind induced stay-cable vibrations", *Proceedings of the 11th International Conference on Wind Engineering, Lubbock*, 2133-2140.

*JH*